Image Anal Stereol 2019;38:245-253 doi:10.5566/ias.2197
Original Research Paper

ENDPOINT DETECTION OF PARTIALLY OVERLAPPING STRAIGHT FIBERS USING HIGH POSITIVE GAUSSIAN CURVATURE IN 3D IMAGES

Markus Kronenberger[✉, 1,2], Katja Schladitz[1], Oliver Wirjadi[1], Christopher Weber[3], Bernd Hamann[4] and Hans Hagen[2]

[1]Image Processing Group, Fraunhofer ITWM, 67663 Kaiserslautern, Germany, [2]Computer Graphics and HCI Group, University of Kaiserslautern, 67663 Kaiserslautern, Germany, [3]Q-DAS GmbH, 69469 Weinheim, Germany, [4]Department of Computer Science, University of California, Davis, CA 95616, U.S.A.
e-mail: markus.kronenberger@itwm.fraunhofer.de, katja.schladitz@itwm.fraunhofer.de, owirjadi@gmail.com, christopherweber80@gmail.com, hamann@cs.ucdavis.edu, hagen@cs.uni-kl.de
(Received June 4, 2019; revised July 23, 2019; accepted July 23, 2019)

ABSTRACT

This paper introduces a method for detecting endpoints of partially overlapping straight fibers in three-dimensional voxel image data. The novel approach directly determines fiber endpoints without the need for more expansive single-fiber segmentation. In the context of fiber-reinforced polymers, endpoint information is of practical significance as it can indicate potential damage in endless fiber systems, or can serve as input for estimating statistical fiber length distribution. We tackle this challenge by exploiting Gaussian curvature of the surface of the fibers. Fiber endpoints have high positive curvature, allowing one to distinguish them from the rest of a structure. Accuracy data of the proposed method are presented for various data sets. For simulated fiber systems with fiber volume fractions of less than 20 %, true positive rates above 94 % and false positive rates below 5 % are observed. Two well-resolved real data sets show a reduction of the first rate to 90.3 % and an increase of the second rate to 13.1 %.

Keywords: endpoint segmentation, image processing, X-ray micro-computed tomography, fiber reinforced polymer.

INTRODUCTION

Composite materials such as glass or carbon fiber reinforced polymers are of practical relevance for a lot of applications. Their macroscopic mechanical properties are significantly affected by the geometric features of the reinforcing fibers. The fiber volume content and local fiber orientation distribution are already accessible non-destructively (Wirjadi *et al.*, 2014). However, other relevant characteristics such as fiber length distribution can be measured only very roughly based on burning the sample and estimating the fiber length distribution from the 2D image of the remaining fibers on a slide (Guo *et al.*, 2005). Approaches for the analysis of fiber lengths from 3D images frequently rely on single fiber segmentation. For this purpose, there exist various approaches. Some of them first perform a segmentation into more parts than intended and trace single fibers afterwards like, e.g., Lux (2013). Other authors directly disconnect touching fibers at their contacts as Viguié *et al.* (2013). An overview is given in previous work (Kronenberger *et al.*, 2018). Unfortunately, images of practically relevant fiber systems usually exhibit much higher fiber volume fractions than those tackled by Altendorf (2012); Weber *et al.* (2012); Lux (2013); Viguié *et al.* (2013). Moreover, resolution is usually chosen such that the imaged volume is representative for the material and does thus in practice not permit single fiber segmentation. Increasing the resolution results in reduced sample size that can render fiber length estimation impossible due to censoring effects. Hence, practically chosen resolutions represent a trade-off and often cause virtually overlapping fibers preventing single fiber separation. Note that fibers can appear slightly overlapping in 3D images, whereas they do not physically overlap. Kuhlmann and Redenbach (2015) suggest an alternative statistical approach estimating the fiber length distribution based on observing uncorrelated fiber endpoints only. In that contribution, Kuhlmann and Redenbach emphasize their need for a robust method for detecting endpoints in 3D images to make their approach practicable. This motivates the work described here.

Nielsen *et al.* (2001) address a similar issue, the detection of so called Koenderink corner points, which means points of locally maximal curvedness. They formalize the relevant mathematical foundations and show that quantities based on principal curvatures are suitable for the detection of extremal points.

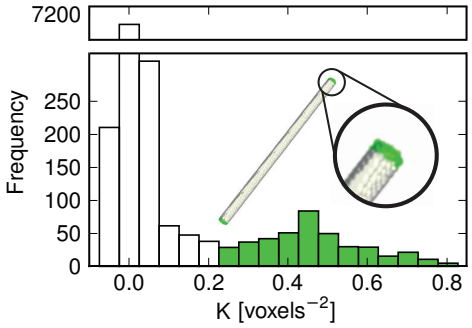

Fig. 1. *Bimodal Gaussian curvature distribution on the surface of a discrete single fiber. The lateral surface of the fiber is flat in one direction leading to curvature values close to zero, whereas slightly spherically shaped ends result in a second peak (colored green).*

Here, we investigate the potential of high positive local Gaussian curvature K to serve as an indicator for fiber ends. This seems reasonable as the lateral surface of a straight or slightly curved fiber is characterized by curvature close to zero, whereas fiber ends exhibit outstandingly positive curvature values (see Fig. 1). The algorithm based on this observation is evaluated using simulated data sets generated by a cherry-pit (Rikvold and Stell, 1985; Torquato, 1991) version of the random sequential adsorption (RSA) algorithm (Feder, 1980) and two real data sets. In summary, this article presents two contributions:

- A novel approach for fiber endpoint identification of partially overlapping straight fibers.
- An accuracy study on fiber systems simulated using a combination of cherry-pit and RSA model as well as two real data sets.

MATERIALS AND METHODS

CHERRY-PIT CYLINDER SYSTEMS

Here, we model fibers with circular cross-sections by straight cylinders and use a modified version of the RSA algorithm to generate 3D images of slightly overlapping cylinder systems. We do this to get closer to what is observable in samples of real fiber reinforced composites. Whereas fibers do not physically overlap, touching fibers can appear slightly overlapping in acquired 3D images. The terms "cylinder" and "fiber" will be used synonymously in the context of this work. The original procedure of RSA reads as follows: Random objects are sequentially added to an initial empty set, under the condition that the newly added objects do not intersect any of the already inserted ones. Within the scope of this work objects are finitely long cylinders with a circular cross-section. In case of a collision, the current object is randomly placed elsewhere and tested again. This is repeated until a given maximum number of insertion attempts a_{max} for one object is violated or the desired total number of objects is reached.

The RSA algorithm produces non-overlapping fibers. However, to simulate slightly overlapping fibers, we adapt the previously described procedure in the following way: Instead of the original radius r of the cylinder being inserted, we use a modified radius $s_{mod} \cdot r$ in the collision test, where s_{mod} is a real number from the interval $]0,1[$. By selecting different values of s_{mod} the degree of overlapping can be adjusted. This procedure is similar to the cherry-pit model known e.g. from Rikvold and Stell (1985); Torquato (1991). The combination is called cherry-pit cylinder model.

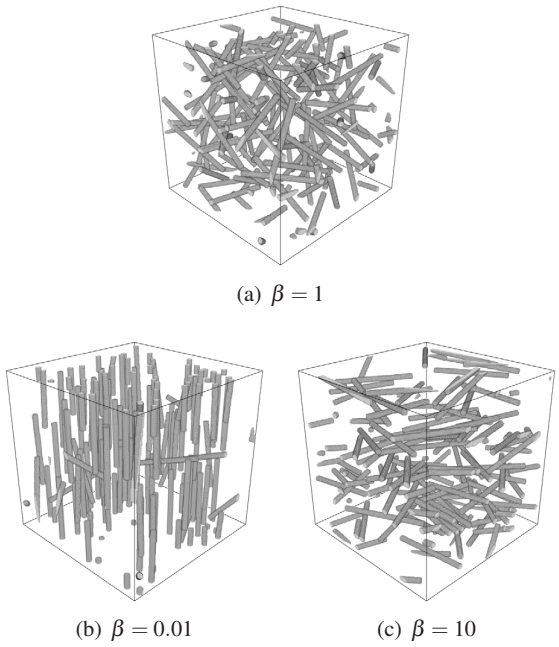

(a) $\beta = 1$

(b) $\beta = 0.01$ (c) $\beta = 10$

Fig. 2. *Realizations of fiber systems with different values of the anisotropy parameter β. (a) shows the isotropic, (b) the bipolar and (c) the girdle case.*

For controlling the orientation distribution of the simulated fibers, we make use of the distribution that is introduced in Schladitz *et al.* (2006); Ohser and Schladitz (2009). Its probability density function is given by

$$\frac{\beta \sin\theta}{4\pi\,(1+(\beta^2-1)\cos^2\theta)^{\frac{3}{2}}},$$

where $\theta \in [0,\pi)$ is the colatitude known from polar coordinates. Note that due to the isotropic behavior in the xy-plane, the longitude has no effect on this distribution. It is a special case of the angular central

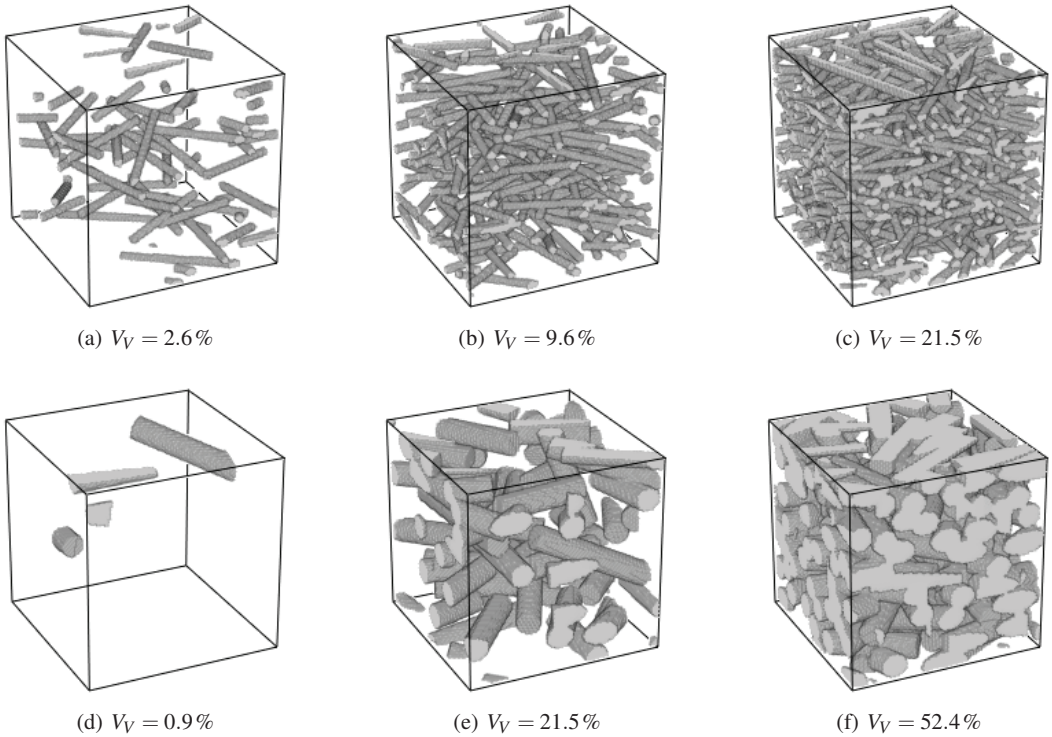

(a) $V_V = 2.6\,\%$ (b) $V_V = 9.6\,\%$ (c) $V_V = 21.5\,\%$

(d) $V_V = 0.9\,\%$ (e) $V_V = 21.5\,\%$ (f) $V_V = 52.4\,\%$

Fig. 3. *Various subvolumes of simulated fiber systems for* $\beta = 10$. *(a) to (c) show systems with a radius* $r = 2$ *voxels, whereas (d) to (f) show examples with* $r = 6$ *voxels. They have a size of* $100 \times 100 \times 100$ *voxels.*

Gaussian distribution and has the advantage that we can specify the type of the distribution by a single parameter $\beta \in (0, \infty)$, which is often referred to as anisotropy parameter. By selecting different values for β, various relevant distributions can be generated: A choice of $\beta = 1$ results in the isotropic case, where orientations are uniformly distributed on the upper-half unit sphere. For a decreasing $\beta < 1$ they concentrate close to the z-axis (bipolar) and for an increasing $\beta > 1$ they tend to be isotropically distributed in the xy-plane (girdle). See Fig. 2 for realizations of fiber systems with different values of β.

A large number of fiber systems is simulated using the cherry-pit cylinder model described above. For all of them we select the number of attempts a_{max} as 250 000, the overlap ratio s_{mod} as 0.6 and the image size as $300 \times 300 \times 300$ voxels. The radius r of the fibers is chosen between 2 and 6 voxels, but constant for one image. This seems reasonable as it roughly reflects what is found in various real fiber systems (Redenbach *et al.*, 2012; Wirjadi *et al.*, 2009; 2014; 2016). For the fiber length, on the other hand, we choose a log-normal distribution with a mean of 50 voxels and a standard deviation of 10 voxels. This seems reasonable since the length should be at least a multiple of the fiber radius, but small compared to the image size.

Regarding the fiber orientation distribution, we simulate fiber systems for all three possible types (bipolar, isotropic and girdle). However, our assumption is that the distribution should not have a significant impact on the endpoint detection as it is based on curvature measurements that are invariant under translation and rotation. Only the frequencies of various overlap configurations differ and therefore could lead to small deviations in the evaluation. See Fig. 3 for some examples of our simulated fiber systems with $\beta = 10$.

FIBER SYSTEMS IN FIBER REINFORCED POLYMERS

Besides simulated fiber systems, we also take real data sets into account. This is necessary as fiber systems contained in samples of real materials often exhibit slight deformations due to fabrication. In order to tackle this aspect in our experiments, we consider two real samples of fiber reinforced polymers.

	Sample 1	**Sample 2**
Image size [voxels]	$350 \times 350 \times 211$	$600 \times 600 \times 300$
Image size [mm]	$0.39 \times 0.39 \times 0.26$	$0.67 \times 0.67 \times 0.33$
Voxel edge length [µm]	1.12	0.79
Fiber volume fraction V_V [%]	14	8
Estimated mean fiber radius [voxels]	4.45	5.62
Estimated β	0.17	4.23

Table 1. *Properties of the real fiber systems shown in Fig. 4.*

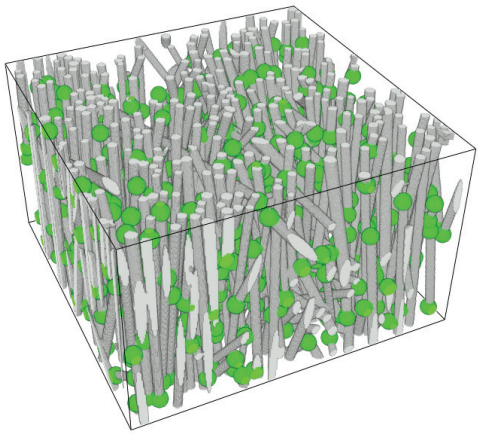

(a) Sample 1

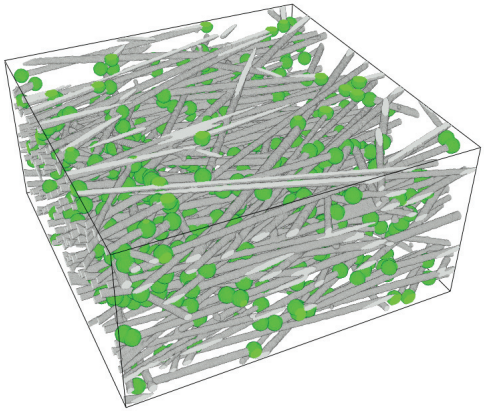

(b) Sample 2

Fig. 4. *Visualizations of two real fiber systems (indicated in gray) together with manually detected fiber endpoints (indicated as green spheres). (a) was imaged by synchrotron micro-computed tomography at ID19 of the European Synchrotron Radiation Facility, Grenoble, France. (b) shows a part of a glass fiber reinforced polybutylene terephthalate plate (Andrä* et al.*, 2019).*

Whereas for synthetic fiber systems exact fiber endpoints are available as a by-product of the simulation, for real fiber systems they have to be manually identified. The complexity of this task varies with the characteristics of the considered samples. In our case we select real samples with a measured mean fiber radius of more than four voxels (see Table 1 for other properties of the data sets). This ensures that fibers are clearly identifiable and a manually detection of endpoints is practicable. To determine the fiber orientation distributions of both data sets, we use the approach proposed by Franke *et al.* (2016). The fiber orientations in the first real data set (sample 1) exhibit a bipolar, whereas in the second data set (sample 2) a girdle distribution. See Fig. 4 for visualizations of their binarized fiber systems that serve as input for our method. In the case of sample 1 we detect 690 and in the case of sample 2 overall 549 endpoints, which seems to be sufficiently large for our subsequent evaluation.

FIBER ENDPOINT DETECTION

DESCRIPTION

The suggested algorithm, given in Table 2, assumes a binary 3D image I_B as input. We consider the 26-neighbourhood, which means that two voxels are neighbors iff their chessboard distance is less than 1.

Step 1 (Gaussian curvature): For each voxel x of the input image I_B the Gaussian curvature K is estimated. To this end, an adapted version of the approach suggested in Kronenberger *et al.* (2015) is applied. The original procedure can be outlined as follows: In each voxel close to the surface, a normal vector is calculated using the local center of mass. The resulting vectors describe the tangent plane in each voxel and are exploited to derive required partial derivatives. Subsequently, the Gaussian curvature is computed by applying a formula based on first and second fundamental form. Finally, all curvature values of a one voxel thick surface layer are extracted.

Here, we replace the procedure for the normal vector computation. In contrast to Kronenberger *et al.* (2015) that uses the center of mass approach, we here

Input: A binary image I_B, the size of a filter kernel σ, a threshold T_C for the Gaussian curvature and a threshold T_V for the minimum size of a detection

1: Estimation of the Gaussian curvature image I_K for I_B controlled by σ
2: Thresholding of I_K using T_C
3: Labeling of connected components
4: Removal of small objects with less than T_V voxels
5: Calculation of the center of mass of each remaining object

Output: A list of coordinates of each detected fiber endpoint

Table 2. *Proposed algorithm to segment fiber endpoints.*

switch to finite differences on a Gauss filtered version of I_B with standard deviation σ. This procedure for estimating normal vectors was proven to be useful also in other application cases (Thirion and Gourdon, 1995; Wernersson *et al.*, 2011). The result of this step is an image I_K containing a curvature value $I_K(x) \in \mathbb{R}$ of each surface voxel x of I_B.

Step 2 (Fiber end extraction): A voxel x is considered to be located at the end of a fiber when its associated curvature value $I_K(x)$ is positive. Whereas in theory a clear distinction between zero and positive curvature values is possible, in the discrete setting of a 3D image, discretization inherent inaccuracies have to be handled (see Fig. 1 as motivation). We tackle this issue by thresholding the curvature image I_K using a user-selected parameter T_C:

$$I_{T_C}(x) = \begin{cases} 1 & \text{if } I_K(x) \geq T_C \\ 0 & \text{otherwise.} \end{cases}$$

In the resulting binary image I_{T_C} the foreground consists of those surface voxels of I_B that are very likely located at fiber ends.

Step 3 (Labeling): For the subsequent steps, it is important that all voxels belonging to the same fiber end are "connected". For this purpose, we label the foreground component of I_{T_C} with respect to 26-connected voxels.

Step 4 (Clean up): Unfortunately, due to artifacts at the fiber surface or noise, not all detections represent real ends. Mostly, false detections consist of a comparably small number of voxels. For this reason, all connected components with less than T_V voxels are removed in this step. See Fig. 5 for an example.

Step 5 (Extraction of coordinates): For applications such as the estimation of the fiber length distribution, fiber end points are more interesting than their geometries. This is the reason why in this last step of the algorithm, the center of mass is calculated for each connected component. These centers are considered as approximation for the endpoints of the fibers. The final output is then a list of these locations.

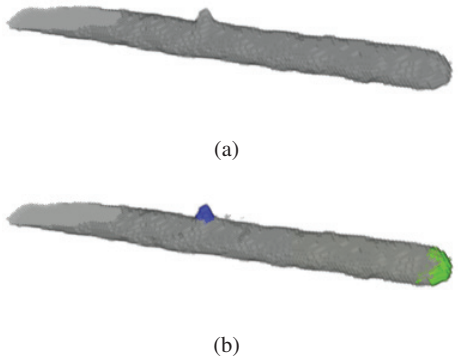

(a)

(b)

Fig. 5. *(a) a cut fiber and (b) detections induced by the proposed approach for* $T_C = 0.02\,voxels^{-2}$ *in different colors. Some noise along the lateral surface produces a false detection shown in blue. It consists of only* 52 *voxels compared to a real fiber end with* 202 *voxels shown in green color.*

RESULTS

True and False Positive Rate

The performance of the suggested approach is evaluated using a concept similar to the receiver operating characteristics (Friedman *et al.*, 2001) as done by Wirjadi (2009). To this end, we define a detection of our algorithm as true positive *TP* if it belongs to an exact endpoint and as false positive *FP* otherwise. See Fig. 6 for a visual explanation of this idea. To determine whether a detection is a *TP* or *FP*, we search for an exact endpoint *EE* that is located nearby, which in our case means not more distant than the fiber diameter d. Using these quantities, we define a true positive rate R_T and false positive rate R_F as

$$R_T = \frac{\sum TP}{\sum EE} \quad \text{and} \quad R_F = \frac{\sum FP}{\sum TP + \sum FP},$$

where $\sum TP$ is the number of true positives, $\sum FP$ the number of false positives and $\sum EE$ the number of exact

fiber ends. R_F is also known as false discovery rate (Benjamini and Hochberg, 1995). In the case of R_T, we nominate $\sum TP$ with $\sum EE$ instead of $\sum TP + \sum FP$ as in our case the number of exact endpoints is available.

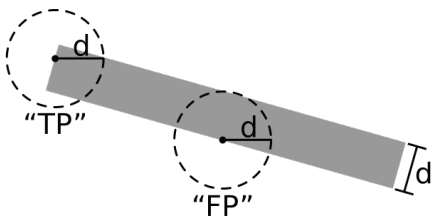

Fig. 6. *Sketch of a 2D fiber with diameter d (shown in gray) and how a true positive and false positive can be interpreted.*

Application to Simulated Fiber Systems

The proposed method for segmenting fiber endpoints is applied to all simulated fiber systems. Fig. 7 present the numerical results of evaluating the estimated fiber endpoints against the ground truth for $\beta = 10$. On the x-axis of each plot, the fiber volume fraction V_V is plotted. On the y-axes of the plots we have the true positive rate R_T and the false positive rate R_F reflecting the accuracy of the approach as well as the input parameters T_C and T_V leading to these rates. The plotted values are the result of an optimization procedure. T_C and T_V are varied until the corresponding value of R_T is maximized under the constraint that R_F is minimal. While doing so we keep the value of σ for the curvature computation constant as 1 for all fiber systems. Other values were tested, but $\sigma = 1$ performed best for simulated fiber systems in our experiment. Whereas in our experiment fiber systems with different fiber orientation distributions (bipolar, isotropic, girdle) are considered, we here only present the result for the bipolar case, as the other two cases do not provide new findings.

In order to increase the visibility of trends, we fit second-degree polynomials through the points of the rates R_T, R_F and first-degree polynomials through the points of the thresholds T_C, T_V. Obviously not all curves cover the same range of fiber volume fractions. This is due to the cherry-pit cylinder model we use. By randomly inserting straight cylinders and allowing only a certain degree of overlap, the space is not completely filled. Hence, the algorithm very quickly reaches a point at which it spends a prohibitive amount of time with insertion attempts and one has to make a compromise between V_V and simulation time. This is of course less severe in the case of the bipolar orientation. Also, in the case of a larger radius the ratio of inserted cylinders and resulting V_V is typically better, because the volume of the individual fibers is higher.

Note that higher fiber volume fractions can be achieved by allowing fibers to bent (Altendorf, 2012). However, in our case straight fibers are intended as it is planed to use their endpoints as input for estimating the fiber length distribution (Kuhlmann and Redenbach, 2015) in the future.

When considering the plots of R_T and R_F, it can be noted that throughout R_T shows a negative and R_F a positive trend when V_V increases. This is also true in the isotropic and girdle case that are not presented here. We can confirm our assumption that the accuracy of the fiber endpoint detection approach is widely independent of the orientation of the fibers, therefore the result of $\beta = 10$ is representative for all three cases. The positive trend of R_T and the negative trend of R_F are plausible, as we allow fibers to overlap and a higher value of V_V simultaneously means a higher number of overlapping fibers. This creates situations in which fiber ends are partially or even completely covered by other fibers and leads to endpoints not found by the suggested approach. Further, it is known that curvature estimators for volume images face problems when objects are lying very close together, as they use small neighborhoods around a voxel for the calculation of the needed normal vectors (Wernersson *et al.*, 2011), which can lead to false positives, too. Another point that should be considered here is the behavior on the image boundary. Fiber ends that are close to the image boundary can produce endpoints that are not found or false positives. All three aspects – overlaps, incorrect curvature estimations and boundary effects – aggravate with increasing fiber volume fraction V_V and thereby explain the trends in the curves of R_T and R_F. We do not exclude boundary effects from our experiment for the following reason. Whereas for simulated data, such effects can be reduced by exploiting the underlying mathematical model, for real data it requires an undesired reduction of the considered part of the image.

When taking a closer look at the plots of the true positive rate R_T and the false positive rate R_F, some further interesting observations can be made. Whereas all curves for radii between 3 and 6 voxels are lying close together, the curves for a radius of 2 voxels show a significant deviation. In the case of R_T, the deviation between the curves increases together with V_V. Until a value of around 10 % for V_V the curves of R_F are indistinguishable, but for higher values the discrepancy becomes visible also in this case. Note that discretization effects become more apparent when the resolution of fibers is lower. Consequently, an accurate estimation of local curvature gets more difficult and

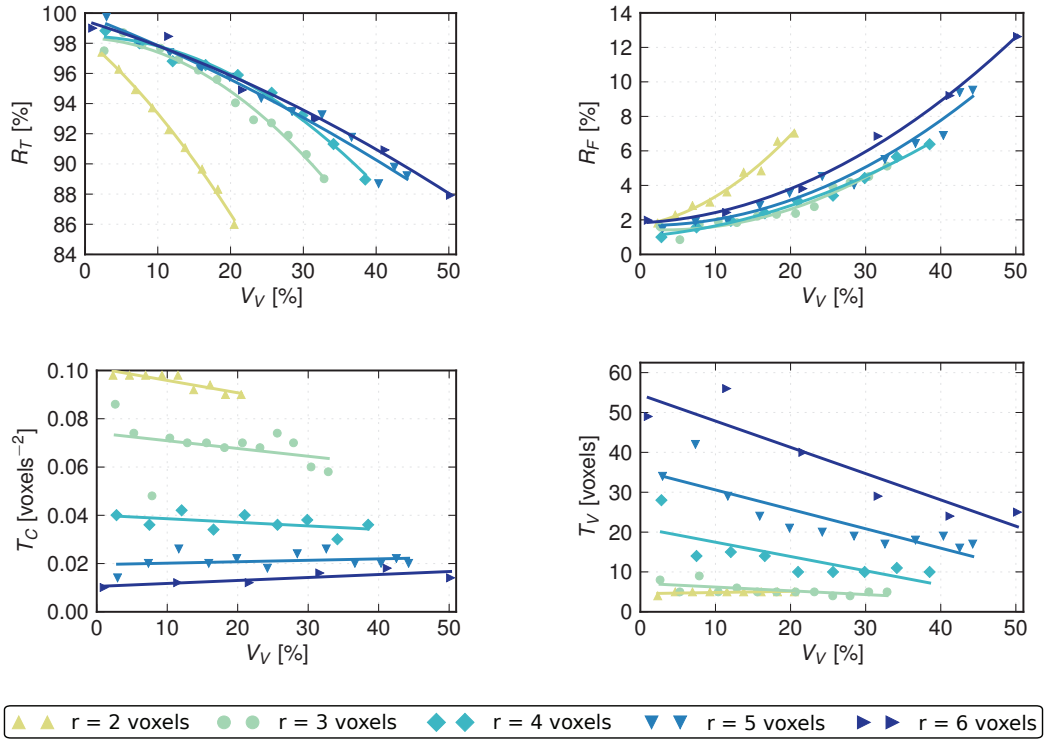

Fig. 7. *Results of our experiment with simulated fiber systems for* $\beta = 10$.

overlaps are more pronounced due to smaller fiber endpoint size.

For simulated fiber systems with a fiber radius of at least 3 voxels and volume fractions less than 20 %, we observe true positive rates above 94 % and false positive rates below 5 %. For V_V larger than 20 % we discuss the results separately, since we no longer have values for R_T and R_F for all radii. For fiber volume fractions between 20 % and 40 %, our proposed method achieves true positive rates above 85 % and false positive rates below 10 % when fibers have a radius of at least 4 voxels.

The plots of the input parameters T_C and T_V show nearly a linear behavior. In the case of the threshold T_C the optimal values change only a little over different fiber volume fractions V_V. Further, it should be noted that with increasing fiber radius the parameter T_C has to be selected smaller. This is reasonable, as for thicker fibers the curvature estimations get more stable and, in addition, the curvature observed at the fiber ends gets smaller.

The curves of the threshold T_V also show the expected behavior. We can report three points worth mentioning. First, with increasing fiber radius also the value of T_V has to be selected higher. This makes sense, as the radius is directly linked to the size of the ends. Second, the points that were computed for larger fiber radii show more pronounced fluctuations. This is reasonable as the choice of T_V has a smaller effect on the result when fiber ends get larger. Third, all lines show a negative trend. As discussed above, a higher fiber volume fraction leads to more overlapping fibers. In order to still be able to detect partly covered fiber ends, the threshold T_V needs to be reduced.

Application to Real Fiber Systems

The proposed method is applied to the two samples shown in Fig. 4. We test different values of σ and optimize R_T, R_F in the same way as described for the simulated data. The results are listed in Table 3. In the case of sample 1 a true positive rate R_T of 97.1 % and a false positive rate of 3.5 % are observed. For sample 2 the results are less accurate. The true positives rate R_T still reaches a high value of 90.3 %, whereas R_F rises to 13.1 %. This high value R_F does not change dramatically when selecting other values of σ. While investigating the corresponding false positives we have found a large number of artifacts on the fiber surface (see Fig. 8). Locally they appear like fiber ends and therefore the suggested approach erroneously detects them. The threshold T_V is intended to tackle this kind of false positives. However, when artifacts and detections of exact fiber ends have similar sizes a

	Sample 1			Sample 2		
	$\sigma = 1$	$\sigma = 2$	$\sigma = 3$	$\sigma = 1$	$\sigma = 2$	$\sigma = 3$
R_T [%]	95	97.1	93.1	87.7	90.3	92.3
R_F [%]	9.6	3.5	6.9	13.7	13.1	15.5
T_C [voxels^{-2}]	0.016	0.014	0.008	0.016	0.010	0.010
T_V [voxels]	80	97	91	101	127	108

Table 3. *Results achieved by applying our approach to the two real fiber systems shown in Fig. 4. Manually segmented endpoints are used as ground truth.*

compromise must be made.

Comparing the thresholds T_C and T_V in Table 3 with the results for simulated fiber systems shown in Fig. 7, the following can be noted. The optimal values of T_C for the real data sets lie slightly below the values determined for the corresponding simulated fiber systems. In the case of T_V the converse behavior is visible. The optimal values of T_V in this experiment are about twice as high as for simulated fiber systems.

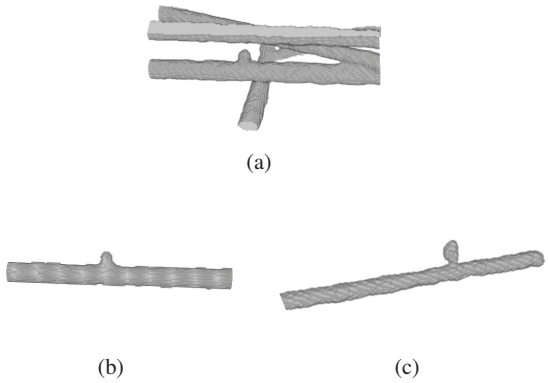

(a) (b) (c)

Fig. 8. *Three examples of artifacts observed for sample 2.*

DISCUSSION

The proposed approach for segmenting fiber endpoints performs well in experiments with simulated fiber systems. True positive rates above 94 % and false positive rates below 5 % for overlapping fibers with a radius between 3 and 6 voxels and fiber volume fractions below 20 % are observed. In the case of the two tested real data sets, the true positive rates go down to a value of 90.3 %, whereas the false positive rates increase to 13.1 % for one of the data sets. The latter observation is structure-related due to artifacts on the lateral surface of fibers whose local shape is identical to a fiber end[1].

ACKNOWLEDGEMENT

This research has been supported by the German research foundation (DFG) within the IRTG 2057 “Physical Modeling for Virtual Manufacturing Systems and Processes” and the Fraunhofer High Performance Center Simulation and Software based Innovation.

REFERENCES

Altendorf H (2012). Analysis and Modeling of Random Fiber Networks. Ph.D. thesis, TU Kaiserslautern, Mines ParisTech.

Andrä H, Dobrovolskij D, Schladitz K, Staub S, Müller R (2019). Modelling of geometrical microstructures and mechanical behaviour of constituents. Berlin, Heidelberg: Springer Berlin Heidelberg, 31–56.

Benjamini Y, Hochberg Y (1995). Controlling the false discovery rate: a practical and powerful approach to multiple testing. J Roy Stat Soc B Met 57:289–300.

Feder J (1980). Random sequential adsorption. J Theor Biol 87:237–54.

Frangi AF, Niessen WJ, Vincken KL, Viergever MA (1998). Multiscale vessel enhancement filtering. In: Proceedings of the First International Conference on Medical Image Computing and Computer-Assisted Intervention, MICCAI ’98. Springer-Verlag.

Franke J, Redenbach C, Zhang N (2016). On a mixture model for directional data on the sphere. Scand J Stat 43:139–55.

Friedman J, Hastie T, Tibshirani R (2001). The elements of statistical learning, vol. 1. Springer series in statistics New York, NY, USA.

Guo R, Azaiez J, Bellehumeur C (2005). Rheology of fiber filled polymer melts: Role of fiber-fiber interactions and polymer-fiber coupling. Polymer Engineering Science 45:385–99.

[1] Frangi’s vessel enhancement filter (Frangi *et al.*, 1998) is able to reduce this effect. However, at the same time, it leads to undesired separations where fibers are touching each other in our experiments.

Kronenberger M, Schladitz K, Hamann B, Hagen H (2018). Fiber segmentation in crack regions of steel fiber reinforced concrete using principal curvature. Image Anal Stereol 37:127–37.

Kronenberger M, Wirjadi O, Freitag J, Hagen H (2015). Gaussian curvature using fundamental forms for binary voxel data. Graph Models 82:123–36.

Kuhlmann M, Redenbach C (2015). Estimation of fibre length distributions from fibre endpoints. Scand J Stat 42:1010–22.

Lux J (2013). Automatic segmentation and structural characterization of low density fibreboards. Image Anal Stereol 32:13–25.

Nielsen M, Olsen OF, Sig M, Sigurd M (2001). Koenderink corner points. In: International Workshop on Visual Form. Springer.

Ohser J, Schladitz K (2009). 3D images of materials structures: Processing and analysis. Chichester: Wiley.

Redenbach C, Rack A, Schladitz K, Wirjadi O, Godehardt M (2012). Beyond imaging: on the quantitative analysis of tomographic volume data. Int J Mater Res 103:217–27.

Rikvold PA, Stell G (1985). Porosity and specific surface for interpenetrable-sphere models of two-phase random media. J Chem Phys 82:1014–20.

Schladitz K, Peters S, Reinel-Bitzer D, Wiegmann A, Ohser J (2006). Design of acoustic trim based on geometric modeling and flow simulation for non-woven. Comp Mater Sci 38:56–66.

Thirion JP, Gourdon A (1995). Computing the differential characteristics of isointensity surfaces. Comput Vision Image Und 61:190–202.

Torquato S (1991). Random heterogeneous media: microstructure and improved bounds on effective properties. Appl Mech Rev 44:37–76.

Viguié J, Latil P, Orgas L, Dumont P, du Roscoat SR, Bloch JF, Marulier C, Guiraud O (2013). Finding fibres and their contacts within 3D images of disordered fibrous media. Compos Sci Technol 89:202–10.

Weber B, Greenan G, Prohaska S, Baum D, Hege HC, Müller-Reichert T, Hyman AA, Verbavatz JM (2012). Automated tracing of microtubules in electron tomograms of plastic embedded samples of caenorhabditis elegans embryos. J Struct Biol 178:129–38. Special Issue: Electron Tomography.

Wernersson ELG, Hendriks CLL, Brun A (2011). Accurate estimation of Gaussian and mean curvature in volumetric images. In: 2011 International Conference on 3D Imaging, Modeling, Processing, Visualization and Transmission.

Wirjadi O (2009). Models and Algorithms for Image-Based Analysis of Microstructures. Ph.D. thesis, Technische Universität Kaiserslautern.

Wirjadi O, Godehardt M, Schladitz K, Wagner B, Rack A, Gurka M, Nissle S, Noll A (2014). Characterization of multilayer structures in fiber reinforced polymer employing synchrotron and laboratory X-ray CT. Int J Mater Res 105:645–54.

Wirjadi O, Schladitz K, Easwaran P, Ohser J (2016). Estimating fibre direction distributions of reinforced composites from tomographic images. Image Anal Stereol 35:167–79.

Wirjadi O, Schladitz K, Rack A, Breuel T (2009). Applications of anisotropic image filters for computing 2D and 3D-fiber orientations. In: Stereology and Image Analysis–10th European Congress of ISS. Milan.